# Imaging Dissolution Dynamics of Individual NaCl Nanoparticles during Deliquescence with *In Situ* Transmission Electron Microscopy

Yuhang Wang,¹ Dewansh Rastogi,²,% Kotiba A. Malek,² Jiayue Sun,¹ Martin Changman Ahn,² Akua Asa-Awuku,¹,²,3,4\* Taylor J. Woehl¹,2\*

- Department of Chemistry and Biochemistry, University of Maryland, College Park, College Park, MD 20742
- Department of Chemical and Biomolecular Engineering, University of Maryland, College Park, College Park, MD 20742
- 3. Department of Civil and Environmental Engineering, University of Maryland, College Park, MD 20742, United States
- Robert E. Fischell Institute for Biomedical Devices, A. James College of Engineering,
  University of Maryland, College Park, MD 20742, United States

\*Corresponding authors: tjwoehl@umd.edu and asaawuku@umd.edu

%Current address: Department of Chemical and Biomolecular Engineering, University of Delaware, Newark, DE 19717

Keywords: in situ transmission electron microscopy, aerosol, deliquescence, crystal dissolution

**Synopsis:** Deliquescence of hygroscopic aerosols is considered an instantaneous process in conventional models. This study utilizes real time nanoscale *in situ* transmission electron microscopy to uncover complex NaCl dissolution dynamics prior to deliquescence.

#### **Abstract**

Water vapor condensation on hygroscopic aerosol particles plays an important role in cloud formation, climate change, secondary aerosol formation, and aerosol aging. Conventional understanding considers deliquescence of nanosized hygroscopic aerosol particles a nearly instantaneous solid to liquid phase transition. However, the nanoscale dynamics of water condensation and aerosol particle dissolution prior to and during deliquescence remain obscure due to a lack of high spatial and temporal resolution single particle measurements. Here we use real time in situ transmission electron microscopy (TEM) imaging of individual sodium chloride (NaCl) nanoparticles to demonstrate that water adsorption and aerosol particle dissolution prior to and during deliquescence is a multistep dynamic process. Water condensation and aerosol particle dissolution was investigated for lab generated NaCl aerosols and found to occur in three distinct stages as a function of increasing RH. First, a < 100 nm water layer adsorbed on the NaCl cubes and caused sharp corners to dissolve and truncate. The water layer grew to several hundred nanometers with increasing RH and was rapidly saturated with solute, as evidenced by halting of particle dissolution. Adjacent cube corners displayed second-scale curvature fluctuations with no net particle dissolution or water layer thickness change. We propose that droplet solute concentration fluctuations drove NaCl transport from regions of high local curvature to regions of low curvature. Finally, we observed coexistence of a liquid water droplet and aerosol particle immediately prior to deliquescence. Particles dissolved discretely along single crystallographic directions, separating by few second lag times with no dissolution. This work demonstrates that deliquescence of simple pure salt particles with sizes in the range of 100 nm to several microns is not an instantaneous phase transition and instead involves a range of complex dissolution and water condensation dynamics.

#### Introduction

Nanosized hygroscopic particles provide nucleation sites for water condensation and droplet growth. Droplet formation involves deliquescence, the phase transition from a solid aerosol to a nano-sized liquid water droplet, followed by spontaneous growth into a micron sized droplet. Atmospheric aerosol particles derive from human activities, including stack emissions, vehicle exhaust, and pesticides, and the natural environment, such as sea spray, dust, and forest fires. These particles undergo a series of complex reactions and eventually form cloud condensation nuclei (CCN), which interact with water molecules in the atmosphere and significantly impact both climate and human health. For instance, CCN concentration impacts cloud structure, which influences Earth's energy balance through albedo, lifetime modulation, and precipitation, playing a crucial role in climate regulation. Additionally, the interaction of respiratory microdroplets carrying pathogens with water vapor impacts respiratory disease transmission. Understanding the interaction of aerosol particles with water vapor is therefore vital to establish accurate models for precipitation, climate change, and aerosol disease transmission.

Hygroscopicity refers to the ability of an aerosol particle to uptake water vapor from air and determines the resulting aerosol particle size as a function of the relative humidity (RH).<sup>11, 12</sup> Many hygroscopic compounds, such as sodium chloride (NaCl) or ammonium sulfate, have a characteristic RH at which they convert from a solid to a liquid drop, termed the deliquescence point. Aerosol particle deliquescence point is typically determined by measuring the ensemble averaged mass growth factor (wet mass/dry mass) as a function of RH.<sup>13</sup> This measurement shows no water uptake below the deliquescence RH and then a discrete jump in mass growth factor upon deliquescence.<sup>14-16</sup> These prior works suggest that deliquescence occurs instantaneously at a given RH and have informed the prevailing assumption of instantaneous aerosol particle dissolution at the deliquescence RH in current aerosol models.<sup>17</sup> However, some recent works have shown that

water condenses on NaCl particles prior to the macroscopic deliquescence point and have measured finite dissolution rates prior to deliquescence. Aerosol salts are generally non-spherical in shape, which is expected to influence the dynamics of water adsorption and particle dissolution in a way that cannot be captured by bulk analysis techniques. The dissolution mechanisms of hygroscopic aerosol particles and the related water condensation dynamics remain obscure due to the lack of single particle measurements.

High spatial and mass resolution single particle measurements, such as *in situ* atomic force microscopy (AFM), electrodynamic balance, optical microscopy/light scattering, and environmental electron microscopy can reveal selected dynamics of water-aerosol interactions. AFM has visualized droplet formation on hygroscopic nanoparticles, but only reveals droplet surface topography with no information about the droplet interior, such as the aerosol particle dissolution dynamics.<sup>22, 23</sup> Optical microscopy can observe particle dissolution and recrystallization, but has a spatial resolution limit of ~500 nm. 14, 24, 25 Electrodynamic balance measures mass growth factor of individual aerosol particles as a function of RH, but provides little information about the aerosol particle morphology or dissolution dynamics during deliquescence. 26-28 Environmental transmission electron microscopy (ETEM) and environmental scanning electron microscopy (ESEM) can image individual hygroscopic nanoparticles with nanometer scale spatial resolution during deliquescence.<sup>29-31</sup> In ETEM the use of differential pumping apertures around the sample region enables keeping the sample, typically a standard carbon coated TEM grid, at a higher pressure (~10 mbar) than the high vacuum in the microscope. Cooling the sample is required to raise the RH to the deliquescence point of hygroscopic salts. Prior ETEM experiments have observed water uptake and shape changes of nanosized aerosol particles prior to the deliquescence point. However, these techniques are limited to low water

partial pressures of ~10 mbar, which is not representative of pressures in the troposphere. Further, prior scanning electron microscopy (SEM) and transmission electron microscopy (TEM) imaging did not provide significant contrast to distinguish between the droplet and aerosol particle, which prevented visualizing and quantifying aerosol particle dissolution dynamics during deliquescence.

In this study, we employ a microelectromechanical system (MEMS) based in situ TEM sample cell to visualize water condensation and dissolution dynamics of cuboid NaCl nanoparticles with single nanometer spatial resolution prior to and during deliquescence.<sup>32-34</sup> Atmospheric aerosols are generally a mix of inorganic and organic compounds and NaCl is representative of highly hygroscopic aerosol particle well-known to readily deliquesce under relevant atmospheric humidity conditions. Real time movies of water condensation and aerosol particle dissolution with increasing RH unveiled complex dynamics prior to deliquescence. The use of scanning TEM (STEM) imaging provided high contrast between the NaCl particle and surrounding water droplet that permitted detailed quantitative analysis of droplet growth and aerosol particle dissolution dynamics. Aerosol particle dissolution and water condensation occurred in three qualitatively distinct stages with increasing RH, including adsorption of a ~100 nm water layer, temporal fluctuations in particle shape, and intermittent dissolution dynamics not previously observed by other single particle methods. This work unveils complex dynamics leading up to deliquescence and challenges the common conception that deliquescence of nanosized aerosol particles is a single-stage instantaneous phase transition. We expect that the in situ TEM methodology established here will become a powerful approach to investigate more complex multicomponent, multiphase aerosols and their interaction with water.

#### **Materials and Methods**

# MEMS sample preparation

The *in situ* TEM cell was composed of two microelectromechanical systems (MEMS) chips, each composed of a silicon base with a 550 x 50 µm hole in the center covered by a freestanding 50 nm thick amorphous silicon nitride film. One chip was patterned with four 500 nm gold spacer posts at the corners to set the chamber height. Each chip was cleaned with acetone and methanol to remove a protective photoresist coating and dried gently with filtered compressed air. The chips were plasma cleaned (Harrick Plasma, PDC-32G) with an air plasma for 45 seconds to remove residual carbon contamination from the solvent. After a wait period of several hours to allow the chips to lose their temporary hydrophilicity, the aerosol particle sample was deposited on the chip that is illuminated by the TEM electron beam first (see in NaCl Sample Preparation). Sample chips with NaCl particles were stored in sealed containers with silica gel desiccant until use.

# NaCl Sample Preparation

Aerosol particles were deposited on MEMS chips using the setup shown in **Figure S1a**. Briefly, a 0.01 g/mL aqueous NaCl (ACS, 99.0% min, Thermo Scientific Chemicals) solution was atomized and the liquid droplet stream was passed through a silica gel diffusion drier to form dry NaCl particles using a sheath flow of filtered room air. The resulting dry NaCl nanoparticles were charged with Krypton 85 and then impacted on an electrically grounded MEMS sample chip supported on a steel mesh. The particle concentration was monitored downstream using an Ultrafine Condensation Particle Counter (TSI 3756 with a detection lower limit of 2.5 nm) and

was found to always be  $> 10^5$  cm<sup>-3</sup>. The deposition time was 4 hours and sample flow rate was 0.3 L/min. The sample chips were stored in a closed container with silica desiccant prior to use.

## In situ TEM

We used a commercially available MEMS based in situ TEM holder with minor modifications for all experiments (Poseidon Plus sample holder, Protochips, USA). The microfluidic lines (PEEK HPLC tubes) in the sample holder were first flushed with 200 proof ethanol, filtered compressed air, and finally dried in a vacuum pump (Pfeiffer Vacuum, USA) overnight to remove residual water and ethanol. The sample holder was then plasma cleaned with an air plasma for 15 minutes to remove residual carbon. A microfluidic gas chamber was formed by sandwiching together two silicon MEMS chips and aligning the imaging windows. The bottom chip was surrounded by a gasket and the top a metal plate, which together hermetically sealed the sample region at near atmospheric pressure (Figure 1a). A leak test was performed in a vacuum pump overnight to guarantee that the sample was hermetically sealed, with the sample reaching a minimum pressure of at least 8.6×10<sup>-5</sup> hPa within 15 minutes. The microfluidic cell initially contained room air with an RH of ~30-40%. The RH in the sample chamber was increased by flowing filtered room air through a water-filled Nafion® humidification tube (Perma Pure, MHTM-Series Humidifiers) into the sample region at a rate of 0.5 mL/s (Figure S1b). The high RH vapor was delivered to the sample chamber via fluid tubes connecting the sample chamber to the back of the sample holder. The RH was measured continuously using an RH meter (Vaisala HMT330 with an error of  $\pm$  2%) at the outlet of the TEM sample holder. However, deliquescence of NaCl occurred at an RH of ~64% as measured at the sample holder outlet, suggesting that this RH measurement was incorrect due to water vapor adsorption in the sample holder. We performed a set of control experiments that showed the RH measured at the gas flow inlet to the sample holder

was consistent with the expected deliquescence RH. We determined a correction factor for the outlet RH measurement,  $1.16 \pm 0.01$ , which was used to correct all RH data (**Figure S2** in Supporting Information). The control experiments for correcting RH for water vapor losses in the microfluidic tubing are described in the Supporting Information. All RH data displayed in this article are expected to have an error of at least  $\pm 2\%$ , which is the instrument error. However, there are other potential sources of error that are difficult to quantify, which are discussed below in the results.

All imaging experiments were performed with a JEOL JEM-2100F operating at 200 kV and 40 pA beam current. Images and in situ movies were captured in bright field (BF) scanning TEM (STEM) imaging mode with a camera length of 10 cm. STEM imaging was utilized because it produces high contrast, high resolution images at low electron fluxes even for relatively thick sample substrates and water layers.<sup>35, 36</sup> The electron flux was calculated by dividing the beam current (in e<sup>-</sup>/s) by the STEM image area to yield a value in e<sup>-</sup>/Å<sup>2</sup> s. Control experiments with NaCl nanoparticles in ~40% RH vapor were performed to establish the optimal imaging magnification range that did not cause electron beam damage to the NaCl (See Supporting Movie 1 for full in situ movie). 37 We found that a magnification of < 100 kX and a dwell time of 5  $\mu s$  did not cause observable damage to NaCl particles with sizes of ~500 – 1000 nm, which corresponds to electron fluxes of < 0.374 e<sup>-</sup>/Å<sup>2</sup> s. *In situ* STEM videos were recorded at a framerate of 10 fps by Camtasia Studios screen capture software and processed in ImageJ and VideoMach. Custom scripts written in MATLAB were used to track the droplet and particle projected area as a function of time and RH in the *in situ* TEM movies. The droplet and particle edge detection had an error of  $\pm 1$  pixel based on visual inspection and comparison of the segmented image and the original image. The script measuring the NaCl surface curvature was adapted from Driscoll et al.<sup>38</sup>

#### **Results and Discussion**

The RH in the sample cell was increased from ambient levels to the deliquescence point of NaCl by flowing humidified air into the sample chamber (**Figure 1a**, **Figure S1**). This procedure of introducing humid air slowly increased RH over several hundred seconds, which contrasts with aerosol instruments that measure steady state aerosol size/mass as a function of RH to track hygroscopic growth. The slow RH increase rate coupled with continuous movie mode imaging allowed observing intermediate states of aerosol particle hydration prior to deliquescence. We repeated the experiment on around 20 different particles over separate three experiments and observed similar phenomena each time.

Aside from the instrument error of  $\pm 2\%$ , temperature fluctuations and the imaging electron beam were the main potential sources of error in the RH measurement. The room temperature was used for RH measurement, which could vary slightly from the sample temperature. However, the TEM instrument room has strict temperature control and the sample was allowed to thermally equilibrate for ~10 minutes after placing in the microscope so this is unlikely to lead to significant error. The previous study by Wang *et al.* showed that the electron beam was able to prompt water vapor condensation by decreasing the local water vapor pressure (increasing the local RH).<sup>39</sup> In this prior study the authors showed that a broad, stationary TEM beam with an electron flux of 0.226 e<sup>-</sup>/Å<sup>2</sup> s induced water condensation from saturated water vapor (RH = 100%). Here we used STEM mode with a smaller electron flux of < 0.1 e<sup>-</sup>/Å<sup>2</sup>s and subsaturated vapor. Taken together, this suggests the electron beam will not promote water condensation. As shown below, several measurements showed that NaCl deliquesces under the electron beam near the accepted value of 75%, suggesting temperature difference and the electron beam did not significantly modify the RH.

Electron beam damage of particles during TEM imaging can be due to knock-on or sputtering damage. For instance, Ott *et al.* showed electron beam damage of ammonium sulfate particles caused formation of circular holes.<sup>37</sup> Supporting Movie 2 shows electron beam damage of an NaCl particle at ~40% RH due to sputtering/knock-on at a magnification of 400 kX (electron flux of 4.15 e<sup>-</sup>/Å<sup>2</sup> s). Electron beam damage to the NaCl particles was not observed for low magnifications (< 100 kX) and electron fluxes (< 0.374 e<sup>-</sup>/Å<sup>2</sup> s) used to collect the data in this study (Supporting Movie 1). As long as magnification was limited to < 100 kX, we did not observe any qualitative differences in the dynamics of the NaCl dissolution and droplet growth.

Hygroscopic growth measurements on aerosolized particles are ideally performed in the aerosol phase; however, a sample substrate was required to image the nanoscale dynamics of particle dissolution and droplet growth. Prior work has shown that the surface could have an impact on the hygroscopic growth.<sup>31</sup> Chatre et al. showed that anisotropic droplets can grow on ammonium sulfate on a hydrophilic surface during imaging with environmental SEM.<sup>31</sup> However, there was no indication in this study that a hydrophilic surface significantly impacted the deliquescence RH. Indeed, several prior studies measured the deliquescence point of salt particles on hydrophobic surfaces and achieved reasonable values. 16, 18, 22 The contact angle of a saturated NaCl solution on the silicon nitride was measured to be  $86 \pm 0.17^{\circ}$  (Figure S3). Control experiments indicated that the SiN surface alone did not condense water. Supporting movie 3 shows that droplets only grew on the salt particles when the RH was approaching the deliquescence point and no droplets formed on the bare SiN. Our experimental deliquescence point was always near 75%, which was close to the literature value. The previous studies and our data strongly suggest the SiN surface did not significantly impact the water uptake dynamics or deliquescence point.

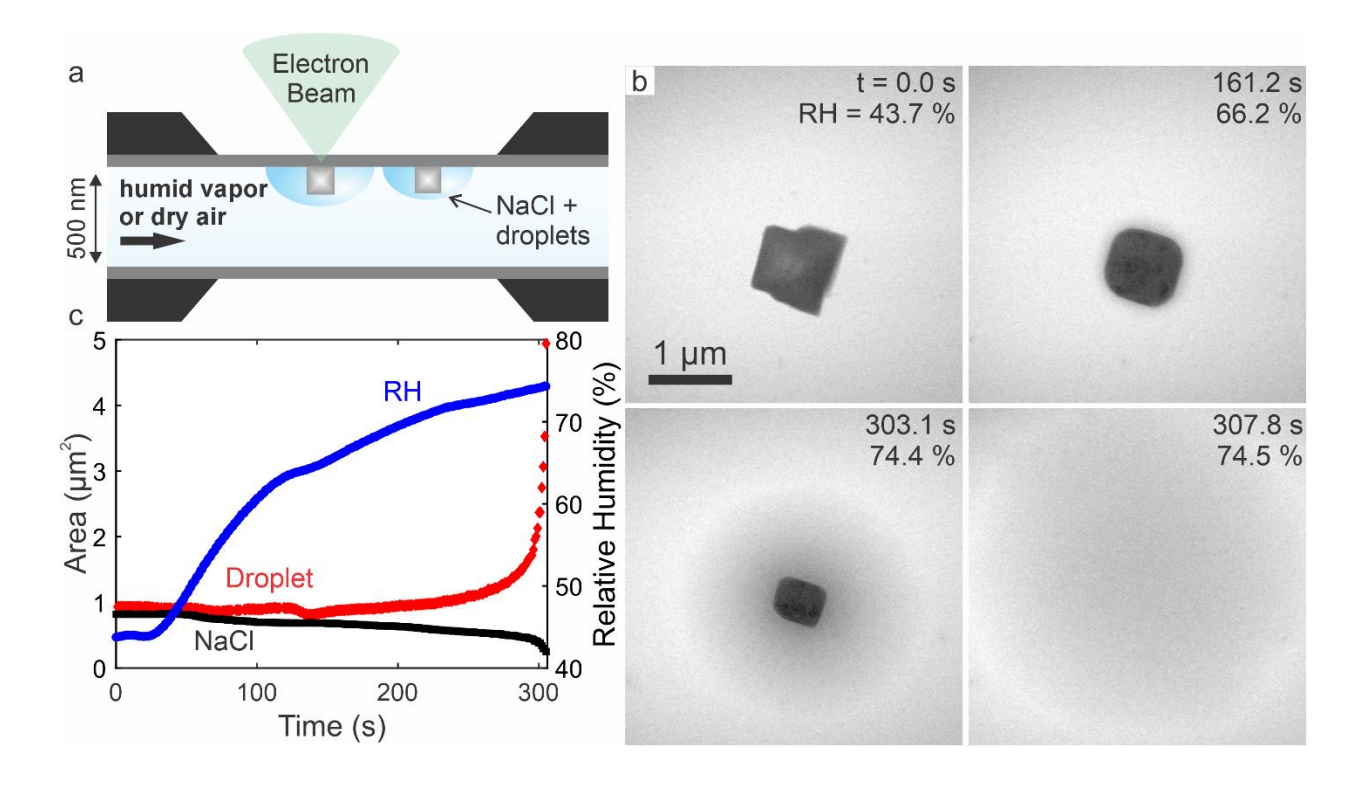


**Figure 1.** *In situ* TEM enables RH control and observation of NaCl deliquescence at room temperature and atmospheric pressure. (a) Schematic of the MEMS sample cell for TEM imaging (not to scale). (b) Time lapsed *in situ* STEM images of the NaCl particle and water droplet as a function of time and RH. (c) Projected droplet area (left axis), projected NaCl area (left axis), and measured RH (right axis) as a function of time. Deliquescence occurred at a time of 308 seconds and RH = 74.5%. Images were acquired at a magnification of 60 kX and electron flux of 0.090 e<sup>-</sup> /Å<sup>2</sup> s. The particle size at t = 0 s was 1010 nm × 960 nm. The error of each length measurement was  $\pm$  10 nm and the error of the area measurement was 0.0139 μm<sup>2</sup>.

Initially, images showed dry NaCl nanoparticles with irregular cuboid shape in contact with 45% RH room air (**Figure 1b**, See Supporting Movie 4 for full *in situ* movie). Increasing RH to 66% caused the sharp corners of the NaCl cubes to dissolve and formed nearly isotropic cubes with truncated corners. A ~100 nm water layer was observed around the NaCl droplet as a lighter 'halo' around the dark contrast particle. As we increased RH to near the deliquescence RH the

water layer grew into a circular droplet (303.1 s) and the NaCl particle dissolved (307.8 s). The slow increase in RH over time and high contrast between the NaCl and water droplet enabled tracking their projected areas with time and RH (Figure 1c). Deliquescence occurred at a measured RH of about 74%, marked by complete dissolution of the NaCl particle and a rapid increase in the growth rate of the water droplet. We compared the growth factor of an NaCl particle as a function of RH to prior measurements by Gupta et al. (Figure 2, Supporting Movie 3). 16 The volume of the particle and droplet cannot be determined from the TEM images, which provide 2D projections of the objects. Instead we utilized the "2D Area Ratio" as implemented by Gupta et al., which is the ratio of the droplet projected area to the initial dry NaCl projected area as determined from optical microscopy images. 16 Interestingly, recasting the 2D area ratio as a function of the RH revealed hygroscopic growth of the NaCl prior to the deliquescence point starting at about RH = 65%, whereas the literature measurements showed essentially no growth until the deliquescence point. The 2D area ratio increased monotonically up to an RH of 74.5%, at which point the NaCl dissolved completely and the liquid droplet grew larger than the image area and could not be measured any longer. We take this point as the deliquescence RH.

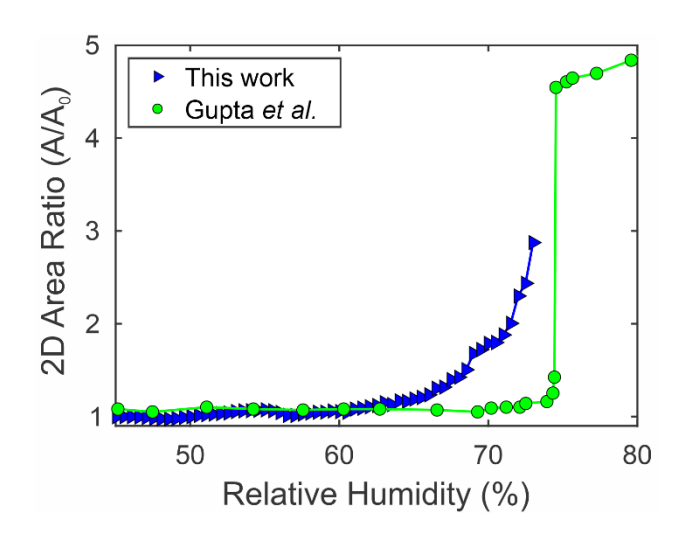


**Figure 2**. 2D area ratio of a single NaCl cube as a function of RH, compared to literature. The experimental single particle measurement by *in situ* TEM is shown by blue triangles and optical microscopy data for micron sized NaCl from literature is shown by green circles. The literature data were reproduced with permission from Gupta *et al*. Copyright 2015 The Authors. <sup>16</sup> The particle size at t = 0 s was 880 nm × 680 nm. The error of each length measurement was  $\pm$  10 nm and the error of the area measurement was 0.011  $\mu$ m<sup>2</sup>.

Careful inspection of the *in situ* TEM movies revealed water condensation and particle dissolution occurred prior to deliquescence via a multistaged dynamic process (Figure 3, See Supporting Movie 4 for full in situ movie). We observed three RH ranges that produced qualitatively different aerosol particle dissolution and water condensation dynamics. The RH ranges of the three stages were defined based on the water layer thickness and dynamics and the NaCl particle shape and dissolution dynamics. We note that the RH range for each condensation stage could vary from particle to particle depending on factors such as initial particle size/shape and RH inaccuracies. Figure 3a shows time lapsed images of an NaCl nanoparticle as a function of RH and time. The first stage of water adsorption spanned an RH range of about 46 - 53% and was characterized by minimal change in the projected area of the NaCl particle (Figure 3b), adsorption of a sub-100 nm water (Figures 3c), and dissolution and rounding of the corners of the NaCl cube. The intensity line profiles of the droplet and NaCl particle in Figure 3c represent the pixel intensities of the line drawn in the 159 s image in Figure 3a. The pixel intensities are inversely proportional to the local density, material thickness, and atomic number of the material in each pixel; the water layer has lower density and thickness (in the beam direction) than the NaCl so it had larger pixel intensity values. The intensity profiles provide information about the shape of the water layer and the NaCl cube in the 3<sup>rd</sup> dimension. Based on the intensity profiles the water

did not form a sessile droplet initially but instead assumed a negative curvature, wetting both the silicon nitride and the NaCl particle (Figure 3d). This was likely because water was found to partially wet the silicon nitride with a contact angle of 86°. It is possible the negative curvature of the region where the NaCl met the silicon nitride encouraged water condensation; however, we could not measure the 3D shape of the NaCl cube or water layer so it is not possible to estimate the local negative curvature. The intensity of the center NaCl remained the approximately same, which suggested that either water did not adhere to the top of the cube or the water layer was very thin. After deliquescence the droplet assumed a sessile droplet shape (t = 268 s). Rounding of sharp corners is consistent with prior ETEM observations and is due to the increased solubility of high curvature corners as described by the Gibbs-Thomson effect.<sup>24,25,40, 41</sup> The second stage of water condensation prior to deliquescence occurred over an RH range of about 54-68%. Here the water layer thickness, observed as an orange halo around the NaCl in the false colored images, increased to between 100 – 200 nm and the curvature of the NaCl cube corners fluctuated in time. The third stage of water condensation occurred at RH > 68% and was distinguished by a monotonic increase in the droplet area and decrease in the NaCl projected area until the aerosol particle completely dissolved. Interestingly, dissolution occurred in discrete steps instead of continuous isotropic dissolution.

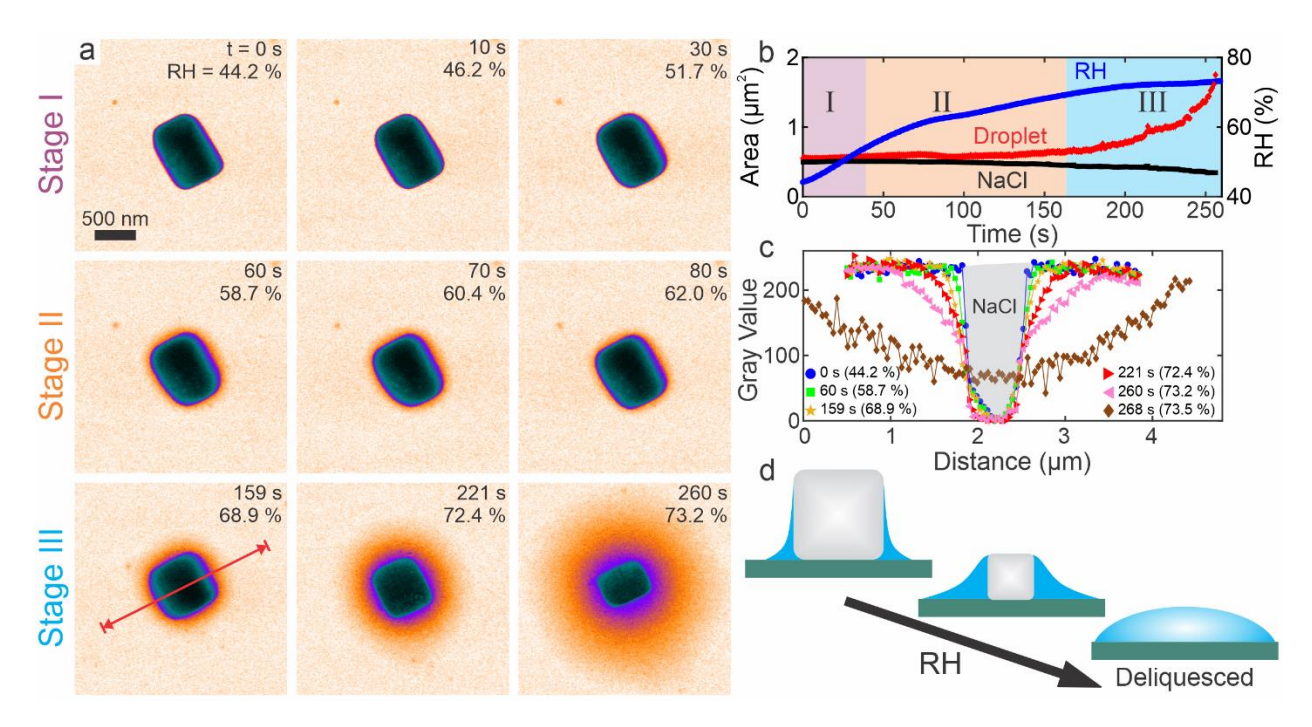
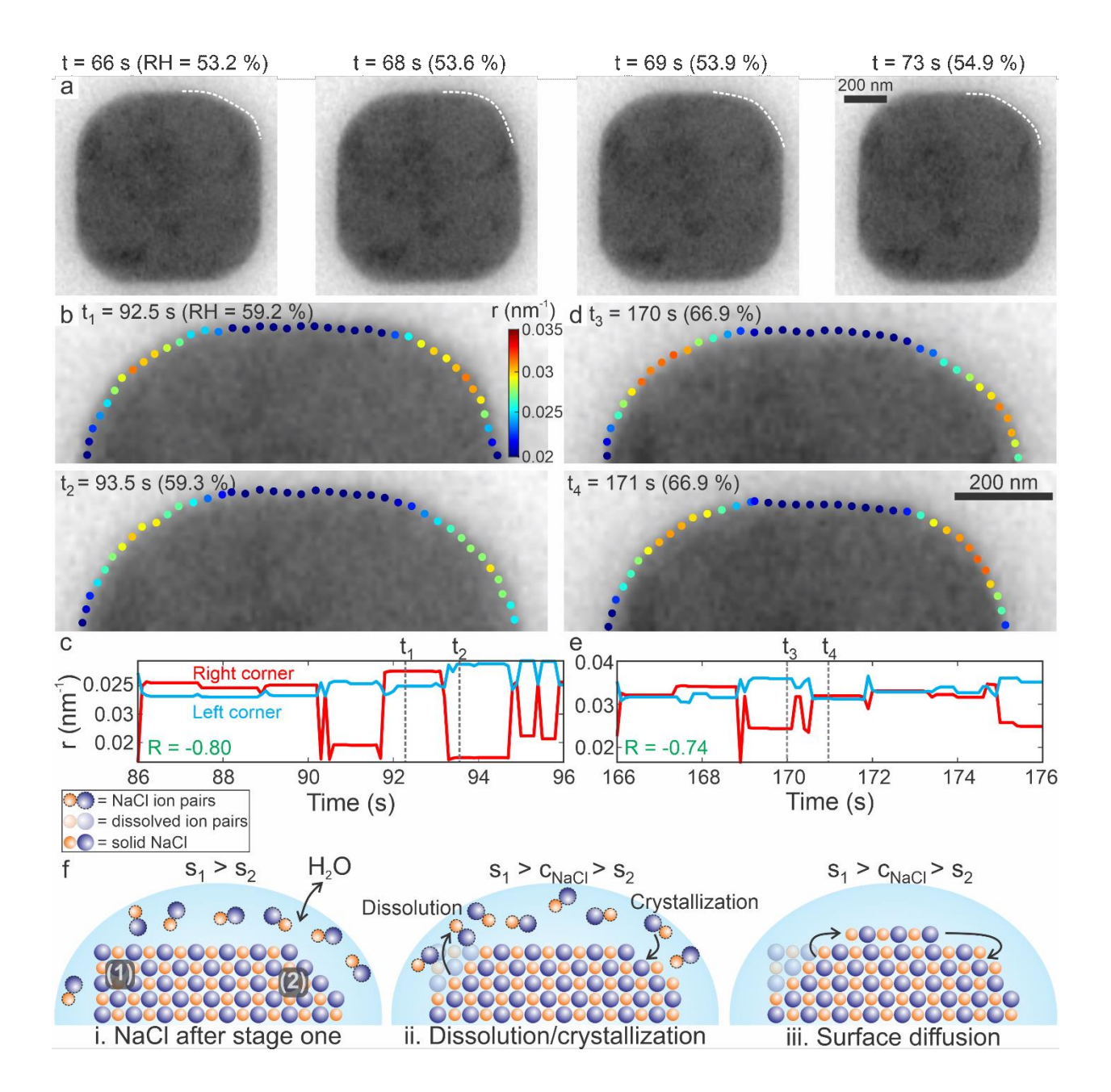


Figure 3. Three stages of water condensation prior to deliquescence. (a) Plan view time lapsed *in situ* BF STEM images of the NaCl as a function of time and RH. The images are false colored to emphasize the water layer, where NaCl appears black/green and the water layer appears orange/purple. Images were acquired at a magnification of 60 kX and electron flux of  $0.090 \, e^{-1}$ Å<sup>2</sup> s. The particle size at t = 0 s was 880 nm × 680 nm. The error of each length measurement was  $\pm$  10 nm and the error of the area measurement was  $0.0111 \, \mu m^2$ . (b) The droplet and NaCl particle projected area and RH as a function of time. The colored background indicates the time and RH range of the three stages of water condensation. (c) Image intensity measured across the line shown in the RH = 68.9% image as a function of time and RH. The gray shaded region represents the position and intensity of the initial NaCl particle at 44.2% RH. (d) Schematic cartoon showing the side view of the water drop profile, where the gray cube is NaCl, blue is water, and green is silicon nitride. The water adopts negative curvature prior to deliquescence and forms a sessile drop after deliquescence.

The second stage of water condensation was investigated in more detail by measuring the NaCl surface curvature as a function of time and RH (Figure 4, See Supporting Movie 4 for full in situ movie). Here the surface curvature (r) is defined as the reciprocal of the radius of the incircle for a given set of points along the surface of the NaCl particle. When determining and comparing cube corner curvature, we note that the terminology, "high" or "low," for corner curvature is relative to the curvature of that corner at a different time or relative to a neighboring corner of the same cube. Figure 4a shows time lapsed in situ BF STEM images of an NaCl cube with the water layer removed by digital background subtraction to isolate the NaCl particle for analysis. Here we observed the top right cube corner curvature fluctuated every few seconds between a low and high curvature state via dissolution and crystallization. There was nearly no change to the particle area during this dynamic process. The curvature change dynamics can be observed very clearly in the in situ STEM movies (Supporting Movies 4-6). We note that all corners of a given cube experienced curvature fluctuations with one or two corners typically showing the largest fluctuations. The corner with the largest curvature fluctuations was different for different particles (Supporting Movies 4-6). Mapping the surface curvature of adjacent cube corners showed that the curvature fluctuations were anticorrelated in time (Figures 4b-e). For instance, the righthand cube corner in Figure 4d showed an increase in curvature that was synchronized in time with a decrease in the left-hand corner curvature (Figure 4d,e). The synchronized increase/decrease in adjacent corner curvature was further evidenced by the negative Pearson's correlation coefficient over these time ranges (inset **Figure 4c,e**). The curvature of non-adjacent corners showed nearly no time correlation (Figure S4).



**Figure 4.** Curvature fluctuations during stage two of water adsorption to NaCl were anticorrelated in time. (a) *In situ* STEM images showing fluctuations in corner curvature with progressively increasing RH. The white dashed lines trace the boundary of the top right corner to highlight changes in curvature. Images were acquired at a magnification of 60 kX and beam current of 40 pA, giving an electron flux of 0.090 e<sup>-</sup>/Å<sup>2</sup> s. (b)-(e) Surface curvature mapping of the same NaCl particle at two different times and RH. (b),(d) (Cropped) STEM images with the local surface

curvature shown as a heat map. (c),(e) The maximum corner curvature as a function of time corresponding to the time ranges in (b) and (d). The inset numbers in green are the Pearson's correlation coefficients calculated for the time ranges of the plots. (f) Schematic illustration of the proposed mechanisms for the corner curvature fluctuation. The particle size at t = 66 s was 970 nm  $\times$  950 nm.

The corner curvature time fluctuations can be explained in terms of curvature-dependent solubility and NaCl concentration fluctuations in the droplet (**Figure 4f**). According to the Gibbs-Thomson effect, the solubility of a solid increases with increasing (positive) surface curvature:<sup>41</sup>

$$c_{NaCl} = c_{\infty} \exp\left[\frac{4\sigma V_m r}{RT}\right],\tag{1}$$

where  $c_{NaCl}$  is the curvature dependent solubility,  $c_{\infty}$  is the bulk solubility,  $\sigma$  is the surface energy of the NaCl,  $V_m$  is the molar volume of solid NaCl. Interestingly, there was minimal change to the projected area of the NaCl particle or water droplet while the RH increased by ~10%. This suggests that the water droplet was saturated with NaCl over this range, halting dissolution. We propose that fluctuations in the NaCl nanoparticle shape were due to small scale fluctuations in local water partial pressure or vapor pressure at the droplet surface, which caused water exchange between the droplet and vapor phase. These fluctuations could be due to small local fluctuations in gas flow rate, temperature, or droplet curvature. Prior work by Wang *et al.* revealed that the local temperature near a condensing water droplet imaged with LP-TEM could fluctuation  $\pm$  10 °C due to electron beam heating and the latent heat of condensation. Likewise, contact line pinning to surface defects or patchy surface chemistry on the silicon nitride could locally change the water curvature, leading to changes in local water vapor pressure. Exchange of water between the vapor and liquid phase in turn decreased or increased the local droplet solute concentration, promoting

crystallization or dissolution depending on local surface curvature. We propose two potential mechanisms—dissolution-crystallization and surface diffusion—by which the NaCl cube could reconfigure its shape in response to local droplet NaCl concentration changes. The dissolution-recrystallization mechanism relies on the slightly asymmetric initial shape of the NaCl (dynamic shape factor of  $1.08^{43}$ ), which causes the corner curvatures to decrease by unequal amounts during the initial corner rounding in stage one of water adsorption (**Figure 4f.i**). The curvature fluctuations of two adjacent corners with unequal curvature occurs *via* exchange of NaCl ions with the droplet in response to fluctuations in the droplet solute concentration. For instance, if the droplet NaCl concentration,  $c_{NaCl}$ , is less than the solubility ( $s_1$ ) of corner 1 (**Figure 4f.ii**) and larger than the solubility of corner 2 ( $s_2$ ), this will cause synchronized NaCl dissolution at corner 1 and crystallization at corner 2. In other words, the droplet is subsaturated near corner 1 and supersaturated near corner 2.

A second potential pathway for the corner curvature fluctuations is surface diffusion of NaCl from regions of high curvature to low curvature (**Figure 4f.iii**). High curvature cube corners have intrinsically higher chemical potential compared to regions of lower curvature.<sup>44</sup> Instead of dissolving into solution, NaCl ion pairs at high curvature regions could respond to local decreases in droplet solute concentration by moving to regions of lower curvature and chemical potential *via* surface diffusion. Deposition of NaCl on the cube faces separating adjacent corners was not observed because the <100> facets are stable and defect free, which introduces a substantial nucleation energy barrier.<sup>45</sup> Instead, NaCl ion pairs moved along the <100> facets, potentially as rapidly diffusing "floating islands,"<sup>45</sup> and deposited on cube corners that contain defects and low coordination number surface sites with low nucleation energy barriers. This proposed mechanism is consistent with the experimentally observed anti-correlation between the curvature of adjacent

corners and the uncorrelated curvature changes of non-adjacent cube corners (**Figure S4**). However, due to the limited spatial resolution of the low dose *in situ* STEM imaging required to prevent electron beam damage, it is not possible at this time to distinguish whether the dissolution-recrystallization or surface diffusion mechanism control the curvature fluctuation dynamics.

Figure 5 displays the dissolution dynamics of an NaCl particle with an initial dry edge length of  $\sim 1 \, \mu m$ . Once the RH was within a few percent of the deliquescence point, the droplet grew rapidly in time and the NaCl cube dissolved concurrently (Figure 5a, see Supporting Movie 4 for full *in situ* movie). Interestingly, the NaCl particle intermittently dissolved in discrete steps with each dissolution step occurring along a single <100> plane, as opposed to dissolving continuously and isotropically along all crystal directions. This is exemplified in the images at the 296 s and 302 s time points and shown by the time dependent NaCl projected area (Figure 5b) and time dependent droplet growth and particle dissolution rates (Figure 5c). The dissolution rate plot in Figure 5c shows that discrete dissolution steps were interspersed by lag times of several seconds where the particle area remained constant. The liquid droplet surrounding the NaCl displayed discrete growth steps that mirrored the particle dissolution steps in time. Correlation analysis of the droplet growth and NaCl dissolution rates showed strong anti-correlation with a Pearson's correlation coefficient of R = -0.84. The terrace-ledge-framework for crystal dissolution predicts that dissolution begins from a defect site at the corner of the NaCl, which then propagates across the crystal face to remove the entire crystal plane. 46 Our observations show that this mechanism can rapidly remove several lattice planes in a few seconds.

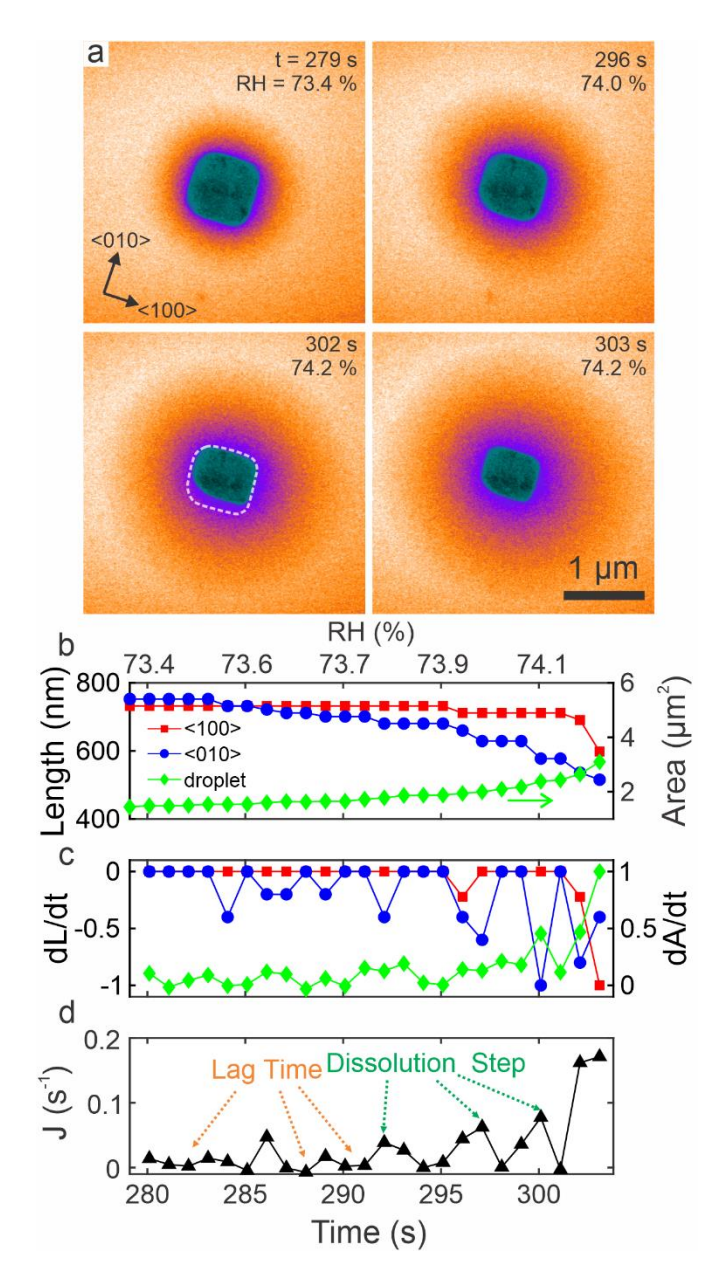


**Figure 5.** Particle dissolution and droplet growth immediately prior to deliquescence were intermittent, leading to co-existence of the NaCl particle and liquid droplet. (a) Time lapsed *in situ* STEM images of concurrent droplet growth and particle dissolution. The images are false colored with the NaCl particle appearing in black/green and the droplet appearing as yellow/purple. Images were acquired at a magnification of 60 kX and electron flux of 0.090 e<sup>-</sup>/Å<sup>2</sup> s. (b)-(d) The top x-axis shows the RH while the lower x-axis shows the time. (b) The projected area of the droplet (green, right axis) and the lengths of the cube along the <100> and <010> axes as defined in (a)

(red and blue, left axis), (c) the instantaneous time derivatives of the droplet area and cube edge lengths (normalized to the maximum values), and (d) the estimated mass normalized dissolution rate of the NaCl particle (J) as a function of time and RH. The error of each edge length measurement was  $\pm$  10 nm and the error of the droplet area measurement was 0.0103  $\mu$ m<sup>2</sup>.

We estimated the mass normalized dissolution rate as a function of time and RH as defined by Ma et al. as  $J = -\frac{dm_{Nact}}{m_{Nact}dt}$ , where NaCl mass was estimated by  $m_{Nact} \approx A_{Nact}^{3/2} \rho_{Nact}$  (Figure 5d). <sup>19</sup> The mass normalized dissolution rate ranged from  $10^{-3} - 10^{-1}$  s<sup>-1</sup> and increased as a function of time and RH, in agreement with the prior measurements by Ma et al. for micron sized NaCl aerosol particles. However, in contrast to the prior work, the *in situ* observations here showed that the instantaneous dissolution rate did not increase monotonically with increasing RH due to the intermittent dissolution process. Instead, this analysis revealed that the average dissolution rate increased with RH due to more frequent and larger dissolution steps. As the RH increased the water condensation rate onto the surface of the droplet increased, decreasing the droplet solute concentration and thus increasing the thermodynamic driving force for crystal defect generation and crystal plane dissolution. Taking the ensemble average over many particles undergoing this discrete dissolution process would indeed be expected to produce an apparent monotonic increase in dissolution rate as observed by Ma et al.

The lag times between discrete dissolution steps partially stemmed from saturation of the water with NaCl, which temporarily halted dissolution. Further RH increases caused additional water condensation and a decrease in the droplet NaCl concentration, which spurred additional dissolution steps. These dynamics contrast dissolution processes in bulk liquid where the solute concentration is nearly constant with time and the particle dissolves continuously.<sup>47-49</sup> Here a

negative feedback loop was established where NaCl dissolution rapidly saturated the liquid droplet and temporarily halted dissolution.

In contrast to conventional understanding of deliquescence, these experiments demonstrate non-instantaneous water uptake on NaCl, where water condenses first as a film on the NaCl surface, followed by formation of liquid droplet that co-exists with a solid NaCl particle.<sup>43</sup> Conventional understanding has considered water absorption as a significant water uptake mechanism only for sparingly soluble and insoluble aerosol particles.<sup>50</sup> Soluble hygroscopic particles are generally considered to uptake water primarily due to solubility-driven hygroscopic growth, i.e., Raoult's law induced decrease in water vapor pressure. <sup>17</sup> This work demonstrates that both water absorption and hygroscopic growth significantly contribute to water uptake on hygroscopic NaCl particles. The Hybrid Activity Model (HAM) for water uptake was developed to consider water uptake by both adsorption and hygroscopic growth.<sup>51</sup> While this model and prior light scattering experiments have suggested water uptake follows this mechanism, the model and measurements could not capture the dynamics of water uptake or particle shape change and dissolution. Our work clearly demonstrates with single particle measurements that water absorption is an important water uptake mechanism for hygroscopic particles. It further demonstrates that empirical single particle measurements are required to understand water uptake and particle dissolution dynamics prior to and at the deliquescence RH.

This work demonstrated direct nanoscale visualization of water vapor condensation on individual NaCl nanoparticles and the subsequent particle dissolution dynamics using a closed *in situ* TEM sample cell with RH control. This *in situ* TEM approach to observing hygroscopic growth of aerosol particles is distinguished from prior measurements by the slow increase in RH with time and continuous movie mode imaging of single nanoparticles, this enabled observing

intermediate states of water condensation and aerosol particle dissolution dynamics prior to deliquescence. Water was observed to interact with NaCl in three qualitatively different stages as the RH was increased from room levels (~40%) to the deliquescence point of ~75%. Initially, a < 100 nm water layer adsorbed on the NaCl and caused preferential dissolution of the sharp cube corners. With increasing RH, a few hundred nanometer water layer deposited on the NaCl and the curvature of adjacent cube corners was observed to fluctuate in time. We proposed dissolution/recrystallization and surface diffusion mechanisms that are consistent with the experimentally observed fluctuation dynamics. Finally, we observed intermittent dissolution of the NaCl particle and co-existence of a solid particle and liquid droplet at RH levels very near the deliquescence point (> 70%). Intermittent dissolution was likely due to saturation of the liquid droplet with NaCl and the slow rate of defect site generation on the NaCl surface. NaCl aerosol is relevant to the atmosphere and well-known for its propensity to swell and form droplets at both sub and supersaturated RH conditions. This work enhances our understanding of deliquescence of hygroscopic aerosol particles using direct nanoscale visualization to unveil complex dissolution phenomena occurring prior to deliquescence, even for highly hygroscopic particles such as NaCl. This concept of water adsorption prior to deliquescence and subsequent multi-step dissolution has been previously postulated, it was mainly attributed to partially water soluble substances. 52, 53 Although particle surface is needed for water condensation, the prevailing theory considers aerosol particle volume and bulk solubility at deliquescence as the sole driver of droplet growth. Recent work here and elsewhere questions these widely used aerosol particle deliquescence theories. Importantly, this work challenges the idea of prompt deliquescence for highly soluble and hygroscopic aerosol particles with visual evidence and emphasizes the need for single particle, nanoscale characterization of dynamic aerosol phase processes.

**Associated content** 

**Supporting Information** 

Experimental apparatus illustrations; RH calibration; Additional curvature fluctuation analysis;

Supporting Movie captions

**AUTHOR INFORMATION** 

**Corresponding Author** 

Taylor J. Woehl – Department of Chemical and Bimolecular Engineering, University of Maryland,

College Park, College Park, MD 20742; <a href="https://orcid.org/0000-0002-4000-8280">https://orcid.org/0000-0002-4000-8280</a>; Phone: 301-405-

1074; Email: tjwoehl@umd.edu

Akua Asa-Awuku - Department of Chemical and Bimolecular Engineering, University of

Maryland, College Park, College Park, MD 20742; https://orcid.org/0000-0002-0354-8368;

Phone: 301-405-8527; Email: asaawuku@umd.edu

**Authors** 

Yuhang Wang - Department of Chemistry and Biochemistry, University of Maryland, College

Park, College Park, MD 20742; Phone: 301-405-1074; Email: yw989898@umd.edu

Dewansh Rastogi - Department of Chemical and Bimolecular Engineering, University of

Maryland, College Park, College Park, MD 20742; https://orcid.org/0000-0002-5416-0048; Phone:

301-405-8527; Email: drastogi@umd.edu

25

**Kotiba A. Malek** – Department of Chemical and Bimolecular Engineering, University of Maryland, College Park, College Park, MD 20742; <a href="https://orcid.org/0000-0002-9326-3859">https://orcid.org/0000-0002-9326-3859</a>; Phone: 301-405-8527; Email: <a href="mailto:kmalek@umd.edu">kmalek@umd.edu</a>

**Jiayue Sun** – Department of Chemistry and Biochemistry, University of Maryland, College Park, College Park, MD 20742; Phone: 301-405-1074; Email: <u>jiaysun@umd.edu</u>

Martin Changman Ahn – Department of Chemical and Bimolecular Engineering, University of Maryland, College Park, College Park, MD 20742; Phone: 301-405-8527; Email: <a href="mainto:mahn1@umd.edu">mahn1@umd.edu</a>

#### **Notes**

The authors declare no competing financial interests.

# **Author contributions**

Yuhang Wang: Conceptualization, Methodology, Software, Validation, Formal analysis, Investigation, Writing — Original Draft, Writing — review & editing, Visualization. Dewansh Rastogi: Conceptualization, Methodology, Validation, Investigation, Writing — review & editing. Kotiba A. Malek: Conceptualization, Methodology, Validation, Investigation, Writing — review & editing. Jiayue Sun: Methodology, Investigation, Writing — review & editing. Martin Changman Ahn: Methodology, Software, Validation, Formal analysis, Investigation, Writing — review & editing. Akua Asa-Awuku: Conceptualization, Methodology, Validation, Resources, Writing — review & editing, Supervision, Funding acquisition. Taylor J. Woehl: Conceptualization, Methodology, Software, Validation, Resources, Writing — review & editing, Visualization, Supervision, Funding acquisition.

#### **ACKNOWLEDGEMENTS**

This work was supported by the National Science Foundation under grant no. 2003927. We acknowledge Sz-Chian Liu in the University of Maryland AIM lab for assistance in TEM operation.

We thank Eiichi Nakamura for helpful discussions on the particle curvature fluctuations.

## References

- (1) Stocker, T. Climate change 2013: the physical science basis: Working Group I contribution to the Fifth assessment report of the Intergovernmental Panel on Climate Change; Cambridge university press, 2014.
- (2) Pierce, J. R.; Adams, P. J. Global evaluation of CCN formation by direct emission of sea salt and growth of ultrafine sea salt. *J. Geophys. Res. Atmos.* **2006**, *111*.
- (3) Sun, J.; Ariya, P. A. Atmospheric organic and bio-aerosols as cloud condensation nuclei (CCN): A review. *Atmos. Environ.* **2006**, *40* (5), 795-820.
- (4) Yu, S. Role of organic acids (formic, acetic, pyruvic and oxalic) in the formation of cloud condensation nuclei (CCN): a review. *Atmos. Res.* **2000**, *53* (4), 185-217.
- (5) Bègue, N.; Tulet, P.; Pelon, J.; Aouizerats, B.; Berger, A.; Schwarzenboeck, A. Aerosol processing and CCN formation of an intense Saharan dust plume during the EUCAARI 2008 campaign. *Atmos. Chem. Phys.* **2015**, *15* (6), 3497-3516.
- (6) Zaveri, R. A.; Wang, J.; Fan, J.; Zhang, Y.; Shilling, J. E.; Zelenyuk, A.; Mei, F.; Newsom, R.; Pekour, M.; Tomlinson, J.; et al. Rapid growth of anthropogenic organic nanoparticles greatly alters cloud life cycle in the Amazon rainforest. *Sci. Adv.* **2022**, 8 (2), eabj0329.
- (7) Bezek, L. B.; Pan, J.; Harb, C.; Zawaski, C. E.; Molla, B.; Kubalak, J. R.; Marr, L. C.; Williams, C. B. Additively manufactured respirators: quantifying particle transmission and identifying system-level challenges for improving filtration efficiency. *J. Manuf. Syst.* **2021**, *60*, 762-773.
- (8) Vejerano, E. P.; Marr, L. C. Physico-chemical characteristics of evaporating respiratory fluid droplets. *J. R. Soc. Interface* **2018**, *15* (139), 20170939.
- (9) Pye, H. O. T.; Ward-Caviness, C. K.; Murphy, B. N.; Appel, K. W.; Seltzer, K. M. Secondary organic aerosol association with cardiorespiratory disease mortality in the United States. *Nat. Commun.* **2021**, *12* (1), 7215.
- (10) Shrivastava, M.; Cappa, C. D.; Fan, J.; Goldstein, A. H.; Guenther, A. B.; Jimenez, J. L.; Kuang, C.; Laskin, A.; Martin, S. T.; Ng, N. L.; et al. Recent advances in understanding secondary organic aerosol: Implications for global climate forcing. *Rev. Geophys.* **2017**, *55* (2), 509-559.
- (11) Razafindrambinina, P. N.; Malek, K. A.; DiMonte, K.; Dawson, J. N.; Raymond, T. M.; Dutcher, D. D.; Freedman, M. A.; Asa-Awuku, A. A. Effects of mixing state on water-uptake properties of ammonium sulfate Organic mixtures. *Aerosol Sci. Techn.* **2022**, *56* (11), 1009-1021.
- (12) Moore, R. H.; Cerully, K.; Bahreini, R.; Brock, C. A.; Middlebrook, A. M.; Nenes, A. Hygroscopicity and composition of California CCN during summer 2010. *J. Geophys. Res. Atmos.* **2012**, *117* (D21), D00V12.
- (13) Dawson, J. N.; Malek, K. A.; Razafindrambinina, P. N.; Raymond, T. M.; Dutcher, D. D.; Asa-Awuku, A. A.; Freedman, M. A. Direct Comparison of the Submicron Aerosol Hygroscopicity of Water-Soluble Sugars. *ACS Earth Space Chem.* **2020**, *4* (12), 2215-2226.
- (14) Li, X.; Gupta, D.; Eom, H.-J.; Kim, H.; Ro, C.-U. Deliquescence and efflorescence behavior of individual NaCl and KCl mixture aerosol particles. *Atmos. Environ.* **2014**, *82*, 36-43.

- (15) Bzdek, B. R.; Walker, J. S. Vibrational spectroscopy of individual aerosol droplets by optical tweezers. *Spectrosc.* **2019**, *34* (4), 22–31-22–31.
- (16) Gupta, D.; Eom, H.-J.; Cho, H.-R.; Ro, C.-U. Hygroscopic behavior of NaCl–MgCl 2 mixture particles as nascent sea-spray aerosol surrogates and observation of efflorescence during humidification. *Atmos. Chem. Phys.* **2015**, *15* (19), 11273-11290.
- (17) Köhler, H. The nucleus in and the growth of hygroscopic droplets. *Trans. Faraday Soc.* **1936**, 32, 1152-1161.
- (18) Wise, M. E.; Martin, S. T.; Russell, L. M.; Buseck, P. R. Water uptake by NaCl particles prior to deliquescence and the phase rule. *Aerosol Sci. Technol.* **2008**, *42* (4), 281-294.
- (19) Ma, S.; Yang, M.; Pang, S.; Zhang, Y. Subsecond measurement on deliquescence kinetics of aerosol particles: Observation of partial dissolution and calculation of dissolution rates. *Chemosphere* **2021**, *264*, 128507.
- (20) Asadzadeh, B.; Bouzidi, H.; Bisson, R.; Ondráček, J.; Schwarz, J.; Lahib, A.; Ždímal, V. Hygroscopicity of secondary marine organic aerosols: Mixtures of alkylammonium salts and inorganic components. *Sci. Total Environ.* **2021**, *790*, 148131.
- (21) Lei, T.; Ma, N.; Hong, J.; Tuch, T.; Wang, X.; Wang, Z.; Pöhlker, M.; Ge, M.; Wang, W.; Mikhailov, E.; et al. Nano-hygroscopicity tandem differential mobility analyzer (nano-HTDMA) for investigating hygroscopic properties of sub-10 nm aerosol nanoparticles. *Atmos. Meas. Tech.* **2020**, *13* (10), 5551-5567.
- (22) Ying, Z.; Zhang, Z.; Zhou, Y.; Wang, Y.; Zhang, W.; Huang, Q.; Shen, Y.; Fang, H.; Hou, H.; Yan, L. Unexpected hygroscopic behaviors of individual sub-50 nm NaNO3 nanoparticles observed by in situ atomic force microscopy. *Sci. Total Environ.* **2022**, *852*, 158441.
- (23) Morris, H. S.; Grassian, V. H.; Tivanski, A. V. Humidity-dependent surface tension measurements of individual inorganic and organic submicrometre liquid particles. *Chem. Sci.* **2015**, *6* (5), 3242-3247.
- (24) Zheludev, N. I. What diffraction limit? *Nat. Mater.* **2008**, 7 (6), 420-422. DOI: 10.1038/nmat2163.
- (25) Sun, J.; Liu, L.; Xu, L.; Wang, Y.; Wu, Z.; Hu, M.; Shi, Z.; Li, Y.; Zhang, X.; Chen, J.; et al. Key Role of Nitrate in Phase Transitions of Urban Particles: Implications of Important Reactive Surfaces for Secondary Aerosol Formation. *J. Geophys. Res. Atmos.* **2018**, *123* (2), 1234-1243.
- (26) Davis, E. J.; Ray, A. Single aerosol particle size and mass measurements using an electrodynamic balance. *J. Colloid Interface Sci.* **1980**, 75 (2), 566-576.
- (27) Lee, A. K.; Ling, T.; Chan, C. K. Understanding hygroscopic growth and phase transformation of aerosols using single particle Raman spectroscopy in an electrodynamic balance. *Faraday Discuss.* **2008**, *137*, 245-263.
- (28) Davies, J. F. Mass, charge, and radius of droplets in a linear quadrupole electrodynamic balance. *Aerosol Sci. Technol.* **2019**, *53* (3), 309-320.
- (29) Wise, M. E.; Biskos, G.; Martin, S. T.; Russell, L. M.; Buseck, P. R. Phase Transitions of Single Salt Particles Studied Using a Transmission Electron Microscope with an Environmental Cell. *Aerosol Sci. Technol.* **2005**, *39* (9), 849-856.
- (30) Wise, M. E.; Semeniuk, T. A.; Bruintjes, R.; Martin, S. T.; Russell, L. M.; Buseck, P. R. Hygroscopic behavior of NaCl-bearing natural aerosol particles using environmental transmission electron microscopy. *J. Geophys. Res. Atmos.* **2007**, *112* (D10), D10224.
- (31) Chatre, C.; Ehret, E.; Ondarçuhu, T.; Steyer, P.; Masenelli-Varlot, K.; Cadete Santos Aires, F. J.; Nozière, B. Influence of Surface-Active Substances and Substrates on the Wettability of

- Individual Aerosol Particles during Condensation by Environmental Scanning Electron Microscopy. *Langmuir* **2023**, *39* (8), 2957-2965.
- (32) Zhang, Q.; Ma, J.; Mei, L.; Liu, J.; Li, Z.; Li, J.; Zeng, Z. In situ TEM visualization of LiF nanosheet formation on the cathode-electrolyte interphase (CEI) in liquid-electrolyte lithium-ion batteries. *Matter* **2022**, *5* (4), 1235-1250.
- (33) Yang, R.; Mei, L.; Fan, Y.; Zhang, Q.; Liao, H.-G.; Yang, J.; Li, J.; Zeng, Z. Fabrication of liquid cell for in situ transmission electron microscopy of electrochemical processes. *Nat. Protoc.* **2023**, *18* (2), 555-578.
- (34) Zeng, Z.; Liang, W.-I.; Liao, H.-G.; Xin, H. L.; Chu, Y.-H.; Zheng, H. Visualization of Electrode–Electrolyte Interfaces in LiPF6/EC/DEC Electrolyte for Lithium Ion Batteries via in Situ TEM. *Nano Lett.* **2014**, *14* (4), 1745-1750.
- (35) Groves, T. Thick specimens in the CEM and STEM. Resolution and image formation. *Ultramicroscopy* **1975**, *I* (1), 15-31.
- (36) de Jonge, N.; Houben, L.; Dunin-Borkowski, R. E.; Ross, F. M. Resolution and aberration correction in liquid cell transmission electron microscopy. *Nat. Rev. Mater.* **2019**, *4* (1), 61-78.
- (37) Ott, E.-J. E.; Kucinski, T. M.; Dawson, J. N.; Freedman, M. A. Use of Transmission Electron Microscopy for Analysis of Aerosol Particles and Strategies for Imaging Fragile Particles. *Anal. Chem.* **2021**, *93* (33), 11347-11356.
- (38) Driscoll, M. K.; McCann, C.; Kopace, R.; Homan, T.; Fourkas, J. T.; Parent, C.; Losert, W. Cell Shape Dynamics: From Waves to Migration. *PLOS Comput. Biol.* **2012**, *8* (3), e1002392.
- (39) Wang, Y.; Rastogi, D.; Malek, K.; Sun, J.; Asa-Awuku, A.; Woehl, T. J. Electric Field-Induced Water Condensation Visualized by Vapor-Phase Transmission Electron Microscopy. *J. Phys. Chem. A* **2023**, *127* (11), 2545-2553.
- (40) Perez, M. Gibbs-Thomson effects in phase transformations. *Scr. mater.* **2005**, *52* (8), 709-712.
- (41) Ma, Q. The gibbs-thomson effect in dilute binary systems. *Metall. Mater. Trans.* **2002**, *33* (4), 1283.
- (42) Wang, M.; Dissanayake, T. U.; Park, C.; Gaskell, K.; Woehl, T. J. Nanoscale Mapping of Nonuniform Heterogeneous Nucleation Kinetics Mediated by Surface Chemistry. *J. Am. Chem. Soc.* **2019**, *141* (34), 13516-13524.
- (43) Biskos, G.; Paulsen, D.; Russell, L. M.; Buseck, P. R.; Martin, S. T. Prompt deliquescence and efflorescence of aerosol nanoparticles. *Atmos. Chem. Phys.* **2006**, *6* (12), 4633-4642.
- (44) Xie, R.; Li, Z.; Peng, X. Nucleation Kinetics vs Chemical Kinetics in the Initial Formation of Semiconductor Nanocrystals. *J. Am. Chem. Soc.* **2009**, *131* (42), 15457-15466.
- (45) Sakakibara, M.; Nada, H.; Nakamuro, T.; Nakamura, E. Cinematographic Recording of a Metastable Floating Island in Two- and Three-Dimensional Crystal Growth. *ACS Cent. Sci.* **2022**, *8* (12), 1704-1710.
- (46) Sangwal, K. Etching of crystals: theory, experiment and application; Elsevier, 2012.
- (47) Li, X.; Qin, F.; Chen, X.; Sheng, A.; Wang, Z.; Liu, J. Dissolution Behavior of Isolated and Aggregated Hematite Particles Revealed by in Situ Liquid Cell Transmission Electron Microscopy. *Environ. Sci. Technol.* **2019**, *53* (5), 2416-2425.
- (48) Liu, L.; Chun, J.; Zhang, X.; Sassi, M.; Stack, A. G.; Pearce, C. I.; Clark, S. B.; Rosso, K. M.; De Yoreo, J. J.; Kimmel, G. A. Radiolysis and Radiation-Driven Dynamics of Boehmite Dissolution Observed by In Situ Liquid-Phase TEM. *Environ. Sci. Technol.* **2022**, *56* (8), 5029-5036.

- (49) Eswara Moorthy, S. K.; Howe, J. M. Kinetic analyses of the growth and dissolution phenomena of primary Si and  $\alpha$ -Al in partially molten Al-Si (-Cu-Mg) alloy particles using in situ transmission electron microscopy. *Metall. Mater. Trans. A* **2011**, *42*, 1667-1674.
- (50) Kumar, P.; Sokolik, I. N.; Nenes, A. Parameterization of cloud droplet formation for global and regional models: including adsorption activation from insoluble CCN. *Atmos. Chem. Phys.* **2009**, *9* (7), 2517-2532.
- (51) Gohil, K.; Mao, C. N.; Rastogi, D.; Peng, C.; Tang, M.; Asa-Awuku, A. Hybrid water adsorption and solubility partitioning for aerosol hygroscopicity and droplet growth. *Atmos. Chem. Phys.* **2022**, *22* (19), 12769-12787.
- (52) Chan, M. N.; Kreidenweis, S. M.; Chan, C. K. Measurements of the Hygroscopic and Deliquescence Properties of Organic Compounds of Different Solubilities in Water and Their Relationship with Cloud Condensation Nuclei Activities. *Environ. Sci. Technol.* **2008**, *42* (10), 3602-3608.
- (53) Peckhaus, A.; Grass, S.; Treuel, L.; Zellner, R. Deliquescence and Efflorescence Behavior of Ternary Inorganic/Organic/Water Aerosol Particles. *J. Phys. Chem. A* **2012**, *116* (24), 6199-6210.

# Table of contents graphic

